Title

Anion capture and exchange by functional coatings: New routes to mitigate steel corrosion in concrete infrastructure

Authors

Falzone, Gabriel
Balonis, Magdalena
Bentz, Dale
et al.

Publication Date

2017-11-01

DOI

10.1016/j.cemconres.2017.08.021

Peer reviewed

Author Manuscript

Accepted for publication in a peer-reviewed journal

NIST National Institute of Standards and Technology • U.S. Department of Commerce

Published in final edited form as:

Cem Concr Res. 2017 November ; 101: 82–92. doi:10.1016/j.cemconres.2017.08.021.

Anion Capture and Exchange by Functional Coatings: New Routes to Mitigate Steel Corrosion in Concrete Infrastructure

Gabriel Falzone[*,†], **Magdalena Balonis**[†,‡,††], **Dale Bentz**[§], **Scott Jones**[§], and **Gaurav Sant**[*,**,††]

[*]Laboratory for the Chemistry of Construction Materials (LC^2), Department of Civil and Environmental Engineering, University of California, Los Angeles, CA, USA

[†]Department of Materials Science and Engineering, University of California, Los Angeles, CA, USA

[‡]Technology Strategist, Institute for Technology Advancement, University of California, Los Angeles, CA, USA

[§]Engineering Laboratory, National Institute of Standards and Technology, Gaithersburg, MD, USA

[**]California Nanosystems Institute (CNSI), University of California, Los Angeles, CA, USA

Abstract

Chloride-induced corrosion is a major cause of degradation of reinforced concrete infrastructure. While the binding of chloride ions (Cl^-) by cementitious phases is known to delay corrosion, this approach has not been systematically exploited as a mechanism to increase structural service life. Recently, Falzone et al. [*Cement and Concrete Research* **72**, 54–68 (2015)] proposed calcium aluminate cement (CAC) formulations containing NO_3-AFm to serve as *anion exchange coating*s that are capable of binding large quantities of Cl^- ions, while simultaneously releasing corrosion-inhibiting NO_3^- species. To examine the viability of this concept, Cl^- binding isotherms and ion-diffusion coefficients of a series of hydrated CAC formulations containing admixed $Ca(NO_3)_2$ (CN) are quantified. This data is input into a multi-species Nernst-Planck (NP) formulation, which is solved for a typical bridge-deck geometry using the finite element method (FEM). For exposure conditions corresponding to seawater, the results indicate that Cl^- scavenging CAC coatings (i.e., top-layers) can significantly delay the time to corrosion (e.g., $5 \leq d_f \leq 10$, where d_f is the steel corrosion initiation delay factor [unitless]) as compared to traditional OPC-based systems for the same cover thickness; as identified by thresholds of Cl^-/OH^- or Cl^-/NO_3^- (molar) ratios in solution. The roles of hindered ionic diffusion, and the passivation of the reinforcing steel rendered by NO_3^- are also discussed.

Keywords

(C) corrosion; (C) finite element analysis; (D) calcium aluminate cement; (D) chloride; (−) calcium nitrate

[††]Corresponding authors: M. Balonis (mbalonis@ucla.edu) and G. Sant (gsant@ucla.edu).

1. Introduction and background

Chloride (Cl^-) induced corrosion of reinforcing steel is a significant cause of premature damage and degradation of concrete infrastructure [1–3]. Concrete may be subject to chloride ingress as a result of contact with de-icing salts, seawater exposure, etc. [4]. In the U.S. alone, over $8 billion is spent annually on corrosion-related repair, maintenance, and rehabilitation of bridges [5]. In addition, 11 % of the 600,000 highway bridges in the U.S. are deemed to be structurally deficient [5,6]; the majority due to corrosion-related degradation.

Due to the alkalinity of cementitious pore solutions, steel embedded in concrete is generally covered with a passivating oxide layer (γ-Fe_2O_3 [7,8]). The ingress of Cl^- ions into the concrete is thought to initiate steel corrosion by displacing OH^- from this passivating layer [2,9]. Cl^--induced depassivation results in localized pitting and corrosion product formation, which reduces the cross-sectional area of the reinforcing steel, and, therefore, its load-bearing capacity [3,7,9]. The Cl^-/OH^- ratio (in molar units), which accounts for the passivating effects of OH^- ions, is often used to describe the risk of steel corrosion [9,10]. Although the precise value of Cl^-/OH^- required to initiate corrosion is a subject of debate [9,10], a survey of the literature suggests that corrosion initiates when $Cl^-/OH^- \geq 0.6$ [9–11].

The presence of NO_3^- and NO_2^- anions in the pore solution can counteract the corrosive actions of Cl^- ions [12–17]. These species mitigate corrosion processes by oxidizing Fe^{2+} species to Fe^{3+} ions, which precipitate and re-form passivating films [7,18]. A critical Cl^-/NO_2^- ratio for corrosion initiation has been suggested to range from 0.25-to-2.0 (unitless, molar ratio) [19,20]. While data regarding NO_3^- is lacking, indirect evidence suggests that NO_3^- provides similar corrosion inhibition as NO_2^- (i.e., for $Cl^-/NO_3^- \leq 0.25$) [21]. While the use of NO_2^- or NO_3^- is valuable, the corrosion inhibition offered by these species offer is often limited by their initial dosage into the concrete [22]. Moreover, both $Ca(NO_3)_2$ and $Ca(NO_2)_2$ are highly soluble and, therefore, are subject to leaching, which may reduce their potential for corrosion mitigation.

The binding of Cl^- by cementitious phases can significantly suppress Cl^-/OH^- in the pore solution and thereby increase the service life of infrastructure [23–25]. For example, Cl^- binding can occur by ion exchange into alumino-ferrite monosubstituent (AFm) compounds, or by sorption onto C-S-H or other compounds [26]. AFm's are represented by $[Ca_2(Al,Fe)(OH)_6]\cdot X \cdot n$H2O, where X is the exchangeable interlayer anion, and n is the number of water molecules. The site (i.e., anion) occupation preference within the AFm-interlayer has the ranking $Cl^- > NO_3^- > NO_2^- > CO_3^{2-} > SO_4^{2-} > OH^-$ [27], assuring that AFm's present in cementitious formulations (i.e., those containing CO_3^{2-}, SO_4^{2-}, or OH^- in their interlayers) will capture Cl^- ions from solution to form Cl-AFm (i.e., Friedel's salt) or Kuzel's salt [27,28]. Ion exchange results in the release of the anion initially present in the AFm interlayer by a process of anion capture and exchange (ACE); a process that is guided by thermodynamic selectivity [27,28].

ACE by AFm's is significant as (i) it operates in a Cl^- concentration range relevant to typical ingress conditions (≈ 14 mmol/L [29]), (ii) it has a much larger binding capacity per

unit mass than Cl^- sorption by C-S-H [25], and (iii) Cl^- species taken up by AFm's are more strongly bound into their structure (i.e., reflecting structural incorporation), than binding by the C-S-H which represents weaker physisorption. Therefore, the Cl^- binding capacity of cementitious formulations is linked to the mass fraction of AFm phases present [30]. Even though the specific binding capacity of AFm phases is high, the total binding capacity of OPC-based formulations is limited, since AFm's comprise only 5 % to 15 % by mass of the solids in a hydrated OPC binder, offering only limited retardation of steel corrosion [19,23–25]. The Cl^- binding capacity of OPC-based binders can be increased by the addition of supplementary cementing materials (SCMs: e.g., ground-granulated blast-furnace slag [31,32], fly ash [33]) which increases the Al_2O_3/SO_3 ratio of the mixture, leading to the enhanced formation of AFm's at the expense of AFt [19,34,35]. However, these effects are confounded with changes in the transport properties (e.g., permeability, and diffusivity) and the limited reaction of the SCMs that become relevant when OPC is replaced by SCMs at high levels [25,34,36]. As a result, while SCMs do indeed contribute reactive alumina that is required for AFm formation, they do so at a level that only slightly increases the mass of AFm's formed.

Several numerical models have been developed to describe mass transport of ions that influence the service life of reinforced concrete infrastructure [23,24,37–42]. These transport models vary in complexity from single-species models governed by Fick's laws of diffusion [23,37], to multi-species Poisson-Nernst-Planck (PNP) models which account for electric coupling between ions due to their differing mobilities [40,41]. Other models may also consider the effect of advective transport due to moisture gradients (e.g., replicating the effects of wet-dry cycles) [43,44] and/or reactions between ions and cementitious solids, which may be accounted for by mass-transport and chemical equilibrium calculations [40,41,45], or by considering sorption isotherms [23,24,37,46]. A wide-range of models especially describe the role of Cl^- binding by cementitious phases on service life predictions [23,24]. Although quantitative prediction of the service lifetime of real structures is notoriously difficult, carefully formulated transport models can illustrate the role of enhanced Cl^- binding by cementitious compounds on delaying the onset of corrosion.

Calcium aluminate cement (CAC) mixtures, when suitably formulated, can exhibit a significantly higher Cl^- binding capacity as compared to those of OPC systems [47]. However, this approach has not been studied as a pathway to mitigate corrosion due to a lack of clarity as to how AFm formation can be increased in a controlled manner to scavenge/sequester Cl^- species. Recently, Falzone et al. suggested that NO_3-AFm dominant hydrated CAC mixtures (e.g., those containing up to 60 mass % AFm) could produce ACE benefits, by sequestering Cl^- ions while simultaneously releasing NO_3^- (or NO_2^-) species, i.e., an anodic corrosion inhibitor [28]. This *smart release* of NO_3^- and NO_2^- ions was first described by Balonis and Glasser [19]. Significantly, since volume changes accompanying NO_3^- to Cl^- exchange in the AFm's are minimal, no internal damage develops, e.g., due to deleterious shrinkage or expansion [48]. With this concept in mind, this study investigates the efficacy of CAC + $Ca(NO_3)_2$ based *top-layers* (i.e., formed by replacing a fractional thickness of the OPC concrete cover) that engender ACE as a means to delay corrosion. CAC-based binders are restricted to a top-layer due to their high cost (≈ 5x that of OPC). The beneficial effects of Cl^- binding (i.e., reduced Cl^- abundance around the steel

reinforcement) and NO_3^- ion release are explained by considering thermodynamic and transport properties that are influential in the initiation and progression of corrosion. As such, this study explains how ACE is an impactful pathway to delay corrosion degradation of infrastructure and thereby prolong service life.

2. Materials and methods

2.1 Materials

A commercially available calcium aluminate cement (Secar®51 produced by Kerneos Aluminate Technologies)[1] was used. The oxide composition of the CAC as determined by X-ray fluorescence (XRF) was (51.05 ± 0.20) % Al_2O_3, (38.94 ± 0.40) % CaO, (4.77 ± 0.40) % SiO_2, (2.23 ± 0.10) % Fe_2O_3, (2.02 ± 0.01) % TiO_2, (0.59 ± 0.10) % MgO, (0.11 ± 0.01) % P_2O_5, (0.31 ± 0.04) % K_2O and (0.07 ± 0.03) % Na_2O by mass [49]. Unless otherwise noted, the uncertainty represents one standard deviation. The mineralogy of the CAC as determined by X-ray diffraction and Rietveld refinement, was 73.3 ± 3.3 % CA, 18.1 ± 3.3 % C_2AS, 4.9 ± 2.0 % CT with minor phases in the form of 0.8 % CaO, 0.6 % C_2F, 1.5 % C_3FT and 0.8 % Fe_3O_4 by mass [50].

CAC pastes were prepared at a fixed water-to-cement ratio (w/c = 0.45, mass basis) using de-ionized (DI) water, as described in ASTM C305 [51]. Calcium nitrate ($Ca(NO_3)_2$, CN) was added to the CAC mixtures in dosages of 0 %, 10 %, and 30 % by mass of anhydrous CAC. The CN admixture was provided in the form of an aqueous solution (52 mass % CN in water). This admixture was first combined with additional water prior to mixing with the anhydrous CAC. CAC mortars were also prepared at the same CN dosages using ASTM C778 [52] compliant graded quartz sand at volume fractions ϕ_q = 0.00, 0.25, and 0.50. To suppress the formation of metastable hydrates [53,54], the mixtures were cured under sealed conditions at 45 °C ± 0.2 °C for a period of 28 d. Reagent grade calcium chloride dihydrate ($CaCl_2 \cdot 2H_2O$, > 99 % purity) was added to Milli-Q water (i.e., 18 MΩ·cm deionized water) to prepare solutions at Cl^- concentrations of: 0.01, 0.05, 0.1, 0.3, 1, and 3 mol/L.

2.2 Methods

2.2.1 Thermodynamic calculations—To ascertain the phase assemblages of the CAC mixtures prepared in Section 2.1, thermodynamic calculations were carried out using the Gibbs Energy Minimization Software[7] (GEMS-PSI), version 2.1 [55–58]. Thermodynamic modeling was performed for systems containing CAC (Secar®51) for w/c = 0.45, and for the three CN dosages listed above [28]. The calculations were carried out at p = 101 kPa and T = 45 °C, with the solid and liquid phases being set to equilibrium with CO_2-free air. The predicted CAC phase assemblages represent mature CAC pastes in which the formation of metastable hydrates CAH_{10} and C_2AH_8 is suppressed [54]. The calculations account for the partial reaction of the anhydrous CAC, to obtain phase assemblages as a function of degree of CAC hydration. The thermodynamic properties of solid and aqueous species were sourced from the GEMS-PSI database, and amended with additional information sourced from the

[1]Certain commercial products are identified in this report to specify the materials used and procedures employed. In no case does such identification imply endorsement or recommendation by the University of California, Los Angeles or the National Institute of Standards and Technology, nor does it indicate that the products are necessarily the best available for the purpose.

literature for CACs [26,27,48,59–63]. Falzone et al. [28] contains further details and a compilation of the thermodynamic properties of compounds relevant to the simulations. Qualitative agreement between GEMS-predicted and experimental phase assemblages for both plain and CN-dosed CAC mixtures has already been established (via X-ray diffraction and thermogravimetric analysis) elsewhere [28].

2.2.2 Cl^- binding isotherms—After 28 d of curing, to minimize transport hindrances on chloride binding, the hydrated CAC pastes were crushed to a fine powder, sieved ($d \leq 63$ μm, d is the particle diameter) and used in Cl^- binding experiments at 25 °C ± 3 °C. Cl^- binding isotherms of CAC pastes dosed with CN admixture (0 %, 10 %, and 30 % by mass) were quantified using the equilibrium method [46]. Triplicate powdered CAC pastes (m_{paste} = 30 g) were immersed in $CaCl_2$ solutions (V_{sol} = 0.1 L) prepared across a range of concentrations [25]. $CaCl_2$ was selected to minimize the potential for cation-dependent alterations to the hydrated phase assemblages, and to provide sufficient Ca^{2+} ions required for the formation of Friedel's salt from hydrogarnet (C_3AH_6) [29,64]. Following immersion of CAC pastes in $CaCl_2$ solutions, the free Cl^- concentration ($C_{Cl,f}$) in solution was measured at 7 d time-intervals over a 21 d period. A multi-parameter benchtop meter (Orion VersaStar, ThermoScientific[1]) that was provided with a Cl^- selective electrode (ISE; 9617BNWP, ThermoScientific[1]) was used to measure $C_{Cl,f}$.

The ISE was calibrated using calibration solutions prepared using Milli-Q water + $CaCl_2.2H_2O$ over the concentration range 0.001 mol/L ≤ $C^0_{Cl,f}$ ≤ 3 mol/L, at 25 °C ± 3 °C. To perform the binding measurements, ≈ 5 mL of solution was extracted, and filtered using a syringe fitted with a 0.2 μm filter to remove solids. The extracted solution was diluted in 100 mL Milli-Q water, and acidified using 0.3 mol/L HNO_3 to adjust the pH to a range of 3 ≤ pH ≤ 4, as required to meet operational specifications of the ISE. The pH was measured using a ThermoScientific Ross Ultra electrode[1] calibrated using buffer solutions over the range 3 ≤ pH ≤ 13 at 25 °C ± 3 °C. To minimize any ionic interferences on the concentration measurement, the solution was then dosed with a suitable amount of ionic strength adjuster (ISA; 2 mL ISA per 100 mL solution), following which $C_{Cl,f}$ was measured using a Cl^- specific ISE.

2.2.3 Static light scattering—Since solid surface area influences binding isotherms, the particle size distributions (PSDs) of the crushed CAC pastes were determined by static light scattering (SLS). An SLS particle analyzer (LS13-320, Beckman Coulter[1]) was used to assess the surface area, using isopropyl alcohol (IPA) as the carrier fluid. Prior to their characterization, each powder was added to IPA and ultrasonicated to ensure its dispersion to primary particles. The complex refractive indices of the IPA and hydrated CAC pastes were taken as n_{IPA}= 1.37+ 0.00i [65] and n_{CAC}= 1.70 + 0.10i [66], respectively. The maximum uncertainty in the median diameter (d_{50}) was around 6 % based on 6 replicate measurements. The d_{50} of the powdered CAC pastes were nominally similar and on the order of 1.3 μm, 1.1 μm, and 2.5 μm for the 0 % CN, 10 % CN, and 30 % CN mixtures, respectively. The densities of these mixtures were estimated as 1700 kg/m^3, 1900 kg/m^3, and 2000 kg/m^3, respectively, based on the thermodynamic calculations. The specific surface

areas of the powders were estimated as 150 m^2/kg, 250 m^2/kg, and 50 m^2/kg, respectively, assuming spherical particles.

2.2.4 Electrical impedance spectroscopy—Electrical impedance spectroscopy was used to assess ion-diffusion in hydrated CAC pastes and mortars based on measurements of their bulk resistance (R_b, ohms) [67]. Custom conductivity cells were fabricated by modifying cylindrical polystyrene containers (diameter = 53.9 mm, height = 47.6 mm). Precision-ground 316 stainless steel rods (diameter = 3.18 mm ± 0.01 mm) served as parallel electrodes spanning the entire height of the container, at a center-to-center separation of 25.4 mm ± 0.5 mm. The geometry factor (k, m^{-1}) of each cell was determined by calibrating the measured conductivity to reference NaOH solutions in DI-water (0.1 % and 5 % by mass).

Hydrated CAC compositions dosed with 0 %, 10 %, 30 % by mass CN and containing different volume fractions of graded quartz sand (ϕ_q = 0.00, 0.25, 0.50) were cast into these cells, sealed, and cured for 28 d at 45 °C ± 0.2 °C; and their bulk electrical conductivity measured in duplicate. EIS spectra were obtained using a Solartron Analytical 1287 Electrochemical Interface[1] with a 1252A Frequency Response Analyzer using an AC input signal of 100 mV. A frequency range of 10^{-1}-to-10^5 Hz was sampled with 10 points recorded per decade.

The effective diffusion coefficient of an ionic species in a cementitious microstructure is related to its bulk conductivity (σ_{eff}; i.e., equivalent to inverse resistivity), and to the conductivity of the solution saturating its pores (σ_0) as described by the Nernst-Einstein relation [68]:

$$D_i = D_i^{inf} \frac{\sigma_{eff}}{\sigma_0} \quad (1)$$

where, D_i^{inf} is the diffusion coefficient of the i^{th} species at infinite dilution in water. This approach was used to account for transport hindrances on chloride (and on nitrate transport), as would be applicable to real concrete systems. As a significant quantity of pore solution from the hydrated CAC pastes [69] could not be obtained, the pore solution conductivity (σ_0) of CAC mixtures (without CN) was calculated based on the initial pore solution concentrations ($I_M \leq 30$ mmol/kg, see Table 1) obtained from GEMS using the Kohlrausch limiting law, with electrochemical activity corrections carried out using the extended Debye-Hückel relation [70]. The conductivity of the pore solutions of the 10 mass % CN and 30 mass % CN mixtures was estimated by performing EIS on solutions with CN dosage equivalent to their mixing water, as the conductivity is expected to be dominated by the abundant CN species.

3. Results

3.1 Thermodynamic calculations

Following on from Falzone et al. [28], Figure 1 shows calculated phase assemblages for CAC pastes (w/c = 0.45) containing different dosages of CN admixture (0-to-30 mass %

CN). In the plain CAC paste (0 % CN, Figure 1a) C_3AH_6, C_2ASH_8, and $Al(OH)_3$ are noted as the predominant hydrated phases. These calculations consider a "mature" CAC paste, meaning that metastable hydrates that could be present at early ages (e.g., CAH_{10}, C_2AH_8) are not expected to exist as they convert, in time (i.e., at equilibrium), to C_3AH_6 and $Al(OH)_3$. When CAC is admixed with a sufficient dosage (30 mass % of CN), C_3AH_6 and C_2ASH_8 formation is entirely suppressed in favor of NO_3-AFm (see Figure 1c). At intermediate CN dosages (e.g., 10 % CN; Figure 1b), the phase assemblage demonstrates an intermediate composition, containing a mixture of NO_3-AFm, C_2ASH_8, and C_3AH_6. These systems are all expected to demonstrate substantial capacity for Cl^- binding, in proportion to their CN dosage. It should be noted that the systems evaluated are water-deficient, meaning that reaction would cease before all the anhydrous CAC is consumed. This is significant as any unhydrated CAC present, in relation to its content, during binding studies (see Section 3.2) will sequester Cl^- by the formation of Friedel's salt. Furthermore, the porosity of the CAC pastes is expected to decrease as the CN dosage increases, due to the larger molar volume of the AFm compounds in comparison to that of C_3AH_6 [28].

3.2 Cl^- binding isotherms

Figure 2 shows the free Cl^- concentration, $C_{Cl,f}$ as a function of time from 0 to 21 d. The solution concentrations are seen to stabilize by 21 d wherein the relative difference in Cl^- concentrations at 21 d and the previous measurement was ≤ 5 % (i.e., within the measurement resolution). Thus, the measured free Cl^- concentrations at 21 d were used to calculate the bound Cl^- content (i.e., expressed in terms of moles of Cl^- bound per kg of hydrated CAC paste) as:

$$C_{Cl,b}^{eq} = \frac{(C_{Cl,f}^{0} - C_{Cl,f}^{21}) \cdot V_{sol}}{m_{paste}} \quad (2)$$

where, $C_{Cl,f}^{0}$ and $C_{Cl,f}^{21}$ represent the concentrations of free Cl^- in solution (in terms of mol Cl^- per L of solution) measured initially, and after 21 d of immersion (t near-equilibrium), respectively.

Figure 3 shows the equilibrium Cl^- binding isotherms for each hydrated CAC paste. The bound Cl^- content is substantially larger for CN-dosed CAC pastes for CN dosage levels ≥ 10 mass %. As expected, the isotherms are non-linear, and demonstrate a plateau in binding at higher Cl^- concentrations. The binding isotherms can be described by a Langmuir expression as [71]:

$$C_{Cl,b}^{eq}(C_{Cl,f}) = \frac{\alpha \cdot C_{Cl,f}}{1 + \beta \cdot C_{Cl,f}} \quad (3)$$

where, $C_{Cl,b}^{eq}$ is the equilibrium bound Cl^- concentration (mol Cl^-/kg CAC paste), $C_{Cl,f}$ is the free Cl^- concentration in solution at equilibrium (mol Cl^-/L solution), and α (L solution/kg CAC paste) and β (L solution/mol Cl^-) are fitting parameters (see Table 2) [46,72]. As a

point of comparison, it should be noted that the Cl^- binding capacity of a typical "neat-OPC" system is approximately 25 % that of the "neat CAC" system shown in Figure 3; at a similar *w/c* and temperature [32].

To better explain the measured Cl^- binding isotherms, the phase assemblages calculated using GEMS were used to estimate the binding capacity of the CAC pastes. Assuming the destabilization of 1 unit of C_3AH_6 (i.e., which occurs at ≈ 0.01 mol Cl^-/L [29]) allows the incorporation of 2 units of Cl^- to form Friedel's salt ($C_3A{\cdot}CaCl_2{\cdot}H_{10}$), C_3AH_6 features a Cl^- binding capacity of 5.36 mol Cl^-/kg C_3AH_6. This binding capacity is greater than that resulting from the uptake of Cl^- into NO_3-AFm (3.10 mol Cl^-/kg NO_3-AFm). This explains why the 0 mass % CN and 10 mass % CN mixtures show similar binding isotherms. But, increasing the CN dosage enhances Cl^- binding in spite of reducing the quantity of C_3AH_6 present by suppressing the formation of C_2ASH_8 (which is not expected to bind Cl^- ions) while enhancing the quantity of NO_3-AFm that is formed; wherein the latter shows significant Cl^- binding by ion exchange.

To discriminate the effects of Cl^- binding via ACE, which releases NO_3^- ions, and binding via C_3AH_6 destabilization (i.e., which does not result in NO_3^- release), the Cl^- binding capacity of each CAC formulation was calculated as the mass-average based on its thermodynamically modeled phase assemblage, and while assuming complete conversion of C_3AH_6 to Friedel's salt. Figure 4 shows the calculated Cl^- binding contributions for each CAC paste overlaid onto its respective Cl^- binding isotherm. The majority of the Cl^- binding isotherm of each CAC paste is explained by its binding capacity calculated based on its predicted phase assemblage. The difference in the measured and calculated isotherms is thought to arise from discrepancies between the thermodynamically modeled phase assemblages and those of the "real" experimental system. However, seeing that this difference increases with CN dosage (i.e., or rather, the quantity of unreacted CAC present; see Figure 3), it is postulated that the difference dominantly results from the reaction between unreacted CAC with Cl^- in solution, and physisorption of Cl^- species onto the residual hydrated phases (e.g., C_2ASH_8). Assuming that C_3AH_6 converts to Cl-AFm before Cl-for-NO_3 exchange by the AFm initiates, the influence of ACE binding can be modeled by a multi-step function. This function equals zero below a critical concentration of free Cl^-, following which it traces the Cl^- binding isotherm. As confirmed by Puerta-Falla et al., Cl-for-NO_3 exchange is set to be equivalent (i.e., to ensure 1:1 monovalent ion exchange) to satisfy conditions of electroneutrality in solution [73].

3.2 Electrical impedance spectroscopy

The EIS response (i.e., a Nyquist plot) of a representative CAC mortar ($\phi_q = 0.50$) for different CN dosages is shown in Figure 5(a). The bulk resistance was quantified as the real component of impedance (Z') at which the imaginary impedance (Z'') displayed a minimum. The bulk electrical conductivity (σ_{eff}, S/m) of the hydrated specimens was calculated as (see Section 2.2.4):

$$\sigma_{eff} = k / R_b \quad (4)$$

Figure 5(b) shows the effective conductivity of CAC mortars as a function of quartz sand volume fraction. At a given quartz volume fraction, the effective conductivity decreases as the CN dosage increases from 0 mass % to 10 mass % CN, and then increases dramatically at the 30 mass % CN dosage. This conductivity minimum is thought to be produced on account of alterations in pore structure/connectivity due to the changes in phase assemblages, although this aspect requires further study. In each case, the bulk conductivity decreases as the volume fraction of quartz sand increases. This is due to dilution of the porous CAC paste matrix, and the reduction in its connectivity (i.e., an increase in tortuosity) due to the presence of non-porous (sand) inclusions [74,75]. This trend is opposite to that observed in OPC mortars, in which ionic diffusivity increases when aggregates are present due to the percolation of the porous interfacial transition zones (ITZ) between the aggregates [74,75]. The values of D_i^{inf} for ions pertinent to seawater are listed in Table 1. The calculated values of σ_0 and the factor σ_{eff}/σ_0 for each cementitious composition are given in Table 2. As a point of reference it should be noted that the CAC mortars feature ionic diffusion coefficients that are equivalent to, or approximately one order of magnitude less than that of a typical OPC concrete [76].

4. Formulation of multispecies reaction-transport model

4.1 Schematic and assumptions

To elucidate the benefits of ACE, a simplified concrete bridge-deck geometry (also representative of a pier with one-face exposed to seawater) was developed. This 1D-domain of a pristine (i.e., uncracked) concrete section is shown in Figure 6. The concrete section has a thickness of $L = 0.2$ m, a fraction of which comprises a CAC-based top-layer of thickness $x_c = 0.025$ m. The depth of the reinforcing steel from the upper surface (i.e., the cover depth) is assumed to be $x_r = 0.050$ m. To describe ion transport, the following assumptions were made:

- The porosity of the concrete and the CAC-based top-layers is saturated with pore solution,
- Advective transport of ions is negligible as a zero pressure gradient is assumed in the pores, hence the pore solution velocity (and Péclet number) is zero, assuming no moisture transport is induced by cyclic wetting-and-drying [43,77],
- The effects of ion-activity (i.e., non-ideality of the solution) on transport are not accounted for since this factor exerts second order contributions to the transport response [78,79],
- The effects of electrical coupling between ions is significant enough to warrant multispecies modeling [42,80], and,
- The electrical double layer present on the hydrated solids does not affect transport [81], since ion transport takes place dominantly through larger capillary pores which remain percolated, rather than through the nanoscale gel pores, e.g., as present in the C-S-H [68].

4.2 Governing equations

For the assumptions noted above, the concentrations of multiple ionic species in solution as a function of space (x) and time (t) can be described by the Nernst-Planck (NP) equation:

$$\frac{\partial C_{i,f}}{\partial t}+\frac{\partial}{\partial x}\cdot\left(-D_i\frac{\partial C_{i,f}}{\partial x}-z_i\frac{D_i}{RT}FC_{i,f}\cdot\frac{\partial\psi}{\partial x}\right)=\upsilon_i \quad (5)$$

where, $C_{i,f}$ is the free concentration of the i^{th} species within the pore solution (mol/L), D_i is the diffusion coefficient of the i^{th} ionic species within the relevant cementitious matrix (m^2/s), z_i is the valence of the i^{th} species, R is the universal gas constant (8.314 J/mol·K), T is the temperature (K), F is Faraday's constant (96484.56 C/mol), ψ is the electric potential (V), and ν_i is the reaction rate of the i^{th} species (mol/(L· s)). The NP equation is governed by the ionic concentrations of n-1 species, where n is the total number of ionic species considered. The concentration of the final (n^{th}) species is governed by the electroneutrality assumption (i.e., zero charge density) which is a simplification of the Poisson equation [82]:

$$\sum_i z_i C_{i,f}=0 \quad (6)$$

The reaction rate (ν_i) in Equation (5) for all species except Cl^- and NO_3^- was assumed to be zero (i.e., no reaction between species). The reaction rates corresponding to the Cl^- and NO_3^- species are expressed by the following first order reactions:

$$\upsilon_{Cl}=k_{Cl}\left(C_{Cl,b}-C_{Cl,b}^{eq}(C_{Cl,f})\right) \quad (7)$$

$$\upsilon_{NO_3}=-k_{Cl}\left(C_{NO_3}^{\max}-C_{NO_3}^{eq}(C_{Cl,f})\right) \quad (8)$$

where, k_{Cl} is the reaction rate constant of Cl-for-NO_3 ion exchange (s^{-1}), and $C_{NO_3}^{\max}$ is the maximum NO_3^- concentration predicted in the pore solution upon exhaustion of the system's ACE capacity. Since Cl^- for NO_3^- exchange in AFm is stoichiometric (i.e., 1 mol Cl^- replaces 1 mol NO_3^-), the molar fluxes of these species are equal and opposite when ACE is the means of Cl^- binding [73]. The Cl^- binding isotherm $C_{Cl,b}^{eq}(C_{Cl,f})$ for any cementitious formulation is given by the Langmuir isotherm parameters noted in Figure 3, scaled to the appropriate units by the paste content and porosity given in Table 2. The binding response, i.e., including the effects of C_3AH_6 conversion, Cl^--for-NO_3^- exchange and the hydration of residual CAC, if any, is given by a piecewise function written as:

$$C_{NO_3}^{eq}(C_{Cl,f}) = \left\{ \begin{array}{ll} 0, & 0\,mol/L \le C_{Cl,f} \le C_{Cl,f}^{A} \\ \frac{\alpha \cdot C_{Cl,f}}{1+\beta \cdot C_{Cl,f}}, & C_{Cl,f}^{A} \le C_{Cl,f} \le C_{Cl,f}^{B} \\ C_{NO_3}^{\max}, & C_{Cl,f}^{B} \le C_{Cl,f} \end{array} \right\} \quad (9)$$

where, $C_{Cl,f}^{A}$ and $C_{Cl,f}^{B}$ are the free Cl^- concentrations at which binding by ACE begins, and ends, respectively. Cl^- binding was modeled as a first-order reaction, in which the driving force is given simply by the difference between the currently bound Cl^- content, and the equilibrium bound Cl^- content predicted by the relevant (mixture dependent) binding isotherm shown in Figure 3. Thus, the following equation was solved for $C_{Cl,b}$:

$$\frac{dC_{Cl,b}}{dt} = k_{Cl}\left(C_{Cl,b} - C_{Cl,b}^{eq}(C_{Cl,f})\right) \quad (10)$$

4.3 Initial and boundary conditions

The concentrations of ions at the exposed surface (i.e., $x = 0$) was set to conform with those of seawater [83]; as noted in Table 1. Table 1 also details the concentrations of ions in the pore solution of the OPC and CAC formulations. The compositions of pore solutions were estimated by thermodynamic calculations (for the CAC formulations) or sourced from the literature (for the OPC system). As expected, the CN-dosed CAC systems show large concentrations of NO_3^- species in their pore solutions, and a pH (OH^- abundance) that is lower than an OPC-concrete system [84].

Assuming ions cannot escape the bottom of the bridge-deck (e.g., due to the presence of stay-in-place metal forms), a zero-flux boundary condition is imposed at $x = L$:

$$N_i(x{=}L) = -\left(D_i\frac{\partial C_i}{\partial x} - z_i\frac{D_i}{RT}FC_i \cdot \frac{\partial \psi}{\partial x}\right) = 0 \quad (11a)$$

where, N_i is the flux of the i^{th} ionic species (mol/m^2·s). Additionally, this lack of "ion escape" also implies electrical insulation (i.e., zero current) at the same boundary:

$$N^{\psi}(x{=}L) = F\sum_i z_i\left(-D_i\frac{\partial C_i}{\partial x} - z_i\frac{D_i}{RT}FC_i \cdot \frac{\partial \psi}{\partial x}\right) = 0 \quad (11b)$$

where, N^{ψ} is the electrical current density (A/m^2). The potential at the exposed surface of the concrete bridge deck was assumed to be zero, i.e., grounded:

$$\psi(x{=}0) = 0\mathrm{V} \quad (12)$$

A perfect bond was assumed between the CAC top-layer and the bulk OPC concrete, and no buildup of electric charge was assumed at the interface. Therefore, ionic flux and electric current density were assumed to be continuous across the interface ($x = L_c$).

Table 2 displays additional material-specific parameters used in the simulations. These include the Langmuir isotherm parameters and reaction rate constants, the factor σ_{eff}/σ_0, porosity and paste content. The maximum uncertainties in α and β were ± 0.0005, and ± 0.0001, respectively. The porosity of each CAC composition was calculated – from its volumetric phase assemblage at a degree of reaction of 70 % – as the fractional volume of the liquid phase present in the system [88]. Although the binding rate constant of Cl^- for NO_3^- exchange in AFm's has been measured to be on the order of $[1.0 \pm 0.2] \times 10^{-5}$ s^{-1}, to improve numerical convergence, the rate constant was estimated as 1×10^{-7} s^{-1} across all compositions [73]. This reduction however, does not significantly influence the results, as the process remains diffusion-limited (i.e., with Damköhler number $\gg 1$) and binding can be approximated as instantaneous. Indeed, over simulated time scales of 1-to-100 years, the simulated Cl^- and NO_3^- concentrations vary by <1% at any x as the binding rate constant is increased (not shown).

4.4 Method of solution

The governing equations (Equations 5 to 10) were solved using the specific initial and boundary conditions (Equations 11–12 and Table 1) within COMSOL Multiphysics 4.3[1], a commercial finite element solver, using the "Chemical Reaction Engineering Module". Numerical convergence was considered to be reached when the highest relative difference in Cl^- concentration profiles was ± 1 %, when reducing the element size or time step by a factor of 2. In practice, converged solutions were obtained by imposing a maximum time step of 1×10^5 s, while using the adaptive time-stepping algorithm built-in to COMSOL and a fixed element size of 5×10^{-4} m.

5. Results of finite element simulations

5.1 Cl^- transport from seawater

The first set of simulations considered surface exposure of an OPC bridge-deck to seawater, the concentration and volume of which remain fixed. Figure 7(a) shows simulated Cl^- concentration profiles within a neat-OPC concrete as a function of distance, x, from the exposed surface. As expected, Cl^- concentrations rise dramatically through the depth of the concrete over time. The corresponding Cl^-/OH^- ratio at various depths in the cover-zone typical for bridge-decks is shown in Figure 7(b).

It is seen that Cl^-/OH^- ratios exceed 0.6 within 30 years; i.e., which would assure corrosion initiation and its progression. Conservatively, the service life of the bridge-deck is defined by the time interval prior to corrosion initiation (t_{init}); i.e., the period in which $Cl^-/OH^- \leq 0.6$. For an OPC cover depth $x_r = 0.050$ m, that is typical for bridge decks, corrosion is expected to initiate for $t_{init} = 6.4$ years. Obviously, increasing the cover depth above steel reinforcement (x_r) to 0.075 m or 0.100 m delays t_{init} to 14.6 years or 25.5 years, respectively. Figure 7(c) displays t_{init} as a function of x_r within an OPC concrete bridge-deck. The

influence of Cl^- binding within the OPC concrete is significant, as a result of which t_{init} approximately doubles for $x_r \geq 0.025$ m. While increasing the cover depth does delay the onset of corrosion, this is often considered as an inefficient and cost-prohibitive mitigation approach.

Second, a scenario was simulated wherein the top 0.025 m of OPC concrete was replaced with a plain CAC mortar top-layer. Figure 8(a) displays Cl^- concentration profiles for such a bridge-deck, wherein the mortar (CAC + 0 % CN) contains a quartz inclusion volume fraction, $\phi_q = 0.50$. In this case, the combined effects of lower ionic diffusivity (≈ ¼ that of OPC concrete) and enhanced Cl^- binding of the CAC top-layer retard Cl^- ingress relative to the OPC concrete (i.e., by increasing t_{init} from 6.4 years to 28.5 years). To highlight these effects on t_{init}, detailed simulations were carried out while assuming: (i) the Cl^- binding capacity of the CAC paste to be similar to the OPC system ($Bind_{top} = Bind_{bulk}$), and, (ii) the ion-diffusivity of the CAC mortar is equivalent to that of the OPC concrete ($D_{top} = D_{bulk}$). The resulting Cl^-/OH^- ratios are displayed in Figure 8(b) for a fixed cover depth, $x_r = 0.050$ m. The reduced ionic diffusivity of the CAC mortar is identified as the primary cause of an increased time to corrosion initiation, as $t_{init} = 18.4$ years solely on the account of retarded ion diffusion (case i, $Bind_{top} = Bind_{bulk}$), while $t_{init} = 9.1$ years when only an increase in Cl^- binding capacity is considered (case ii, $D_{top} = D_{bulk}$). Nevertheless, the effects of enhanced Cl^- binding are significant. When the effects of enhanced binding are negated (i.e., by setting $Bind_{top} = Bind_{bulk}$), Cl^- concentrations in solution are greater as compared to when enhanced binding and reduced diffusivity function in tandem. This clearly indicates the potential benefits of enhanced Cl^- binding in increasing service life.

To further compare the efficacy of CAC top-layers in corrosion mitigation, a corrosion delay factor (d_f) was defined as $d_f = t_{init}(\text{CAC})/t_{init}(\text{OPC concrete})$. Figure 8(c) displays the corrosion delay factor as a function of the reinforcement cover depth in the 0 % CN CAC case. In each case, the corrosion delay factor shows a maximum for $0.01 \text{ m} \leq x_r \leq 0.03$ m, illustrating an optimal efficacy of the CAC top-layer thickness relative to the depth of reinforcing steel. Maximum delay factors range from 2.9 to 13.9, depending on the parameters imposed. It should be noted that these outcomes are broadly independent of the critical Cl^-/OH^- ratio at which corrosion initiates. This is because the critical Cl^-/OH^- ratio influences the magnitude of t_{init}, but only weakly affects d_f.

The effects of CN additions to CAC's were also investigated. Figure 9(a) shows calculated Cl^-/OH-ratios at $x_r = 0.050$ m when an OPC-concrete is topped with a CAC top-layer dosed with 30 mass % CN. The coupled effects of (very slightly) reduced ion-diffusion and substantially enhanced Cl^- binding dramatically hinders Cl^- transport in comparison to OPC concrete. In fact, the 30 % CN composition shows a greater delay efficacy than the 0 % CN composition, despite the fact that its ionic diffusivity is 3x higher. This indicates that the benefits of amplified Cl^- binding capacity of the 30 % CN system far outweighs its increased diffusivity. Unlike the 0 mass % CN case, in which the ion-diffusivity reduction plays a prominent role, enhanced Cl^- capture and the associated NO_3^- exchange are observed to be the dominant mechanisms of corrosion delay. Due to the similarity of the diffusivity within the CAC mortar and OPC concrete, when Cl^- binding within the CAC top-layer is equated to that of OPC (Figure 9a, $Bind_{top} = Bind_{bulk}$); Cl^- ingress is only slightly

reduced, resulting in a predicted time to corrosion of t_{init} = 8.9 years at a cover depth x_r = 0.050 m (i.e., when $Cl^-/OH^- \leq 0.60$). However, due to the high initial NO_3^- concentration in the pore solution, and NO_3^- exchange enabled by the NO_3-AFm, the time to corrosion is expected to be extended.

For clarity, Figure 9(b) displays the relevant Cl^-/NO_3^- ratios as a function of time. When both ionic diffusivity and binding effects are considered, the presence of NO_3^- in the pore solution extends t_{init} to 50.2 years (i.e., when $Cl^-/NO_3^- \geq 0.25$). But, when Cl^- binding is equivalent to the OPC system (i.e., $Bind_{top} = Bind_{bulk}$), Cl^-/NO_3^- quickly exceeds the critical passivation ratio resulting in corrosion initiation. In this case, the presence of NO_3^- does not improve service life, as the time period when $Cl^-/NO_3^- \leq 0.25$ is less than that at which $Cl^-/OH^- \leq 0.6$. These findings are supported by the significant increase in the corrosion delay factor (e.g., see Figure 9c) which exceeds 65 due to the combined effects of reduced diffusivity and enhanced ACE, as compared to only 3 when the effects of enhanced ACE are neglected.

5.2 Parametric study

To deconvolute the effects of enhanced Cl^- binding, reduced ionic diffusivity, and of NO_3^- release (i.e., simultaneous anion capture and exchange) on the time to corrosion initiation, a parametric study was carried out. The simulations considered CAC top-layers with 0 %, 10 %, and 30 % by mass CN, with binding isotherms corresponding to Figure 3; but with an ionic diffusivity equal to that of the OPC concrete. Figure 10(a) displays the corrosion delay factor (d_f) that is predicted for these conditions as a function of the fraction of cover depth composed of CAC (x_c/x_r); for a cover depth x_r = 0.050 m. To set the performance of the baseline scenario, the time to steel corrosion initiation for the OPC concrete system is determined to be 6.4 years.

For all CAC compositions, increasing the CAC layer thickness increases the time to steel corrosion initiation, resulting in corrosion delay factors > 1. For example, when 0.050 m of OPC cover is replaced by a 0 mass % CN CAC mortar top-layer, the time to corrosion initiation doubles. As the CN dosage increases, the provision of CAC top-layers increasingly extends the time to steel corrosion initiation. This is largely due to the release of the NO_3^- ions via ACE ensuring that the $Cl^-/NO_3^- \leq 0.25$. To carefully illustrate the benefits of NO_3^- release in the CAC + 10 mass % CN top-layer, the NO_3^- reaction rate (i.e., ν_{NO3}, Equation 8) was set to zero. In this case, due to the insufficient concentration of free NO_3^- in the pore solution, the service life predicted by the Cl^-/OH^- ratio exceeds that predicted by the critical Cl^-/NO_3^- ratio. However, due to enhanced Cl^- binding, the time to achieve the critical Cl^-/OH^- ratio (Figure 10) is significantly extended relative to the OPC concrete. Despite the similarity between their Cl^- binding isotherms, the CAC + 10 mass % CN top-layer demonstrates larger delay factors than the 0 mass % CN CAC mortar top-layer. This can be attributed to the lower porosity and the higher paste content in the CAC + 10 mass % CN system, which increases the amount of CAC paste available for Cl^- capture from the pore solution. While the effects of enhanced Cl^- capture in this system are substantial, the corrosion delay factor is only one-half of that when ACE (NO_3^- release) is considered.

To examine the benefits of ACE over a wider range of surface Cl^- concentrations, i.e., beyond just seawater exposure, a broader set of simulations were carried out. Here, electroneutrality in the solution at the surface was maintained by modifying the Na^+ concentration concurrently with that of Cl^- (i.e., assuming NaCl as the Cl^- source) – and the thickness of the CAC top-layer was fixed at 0.025 m, while the total cover depth was 0.050 m. Once again, the effects of Cl^- binding and NO_3^- release were separated from that of ion-transport (i.e., diffusion) by setting the diffusion coefficient of the CAC layers equivalent to that of the bulk OPC concrete. The resulting corrosion delay factor is shown as a function of the surface Cl^- concentration (C^S_{Cl}); from 0.1 mol/L to 5 mol/L (Figure 10b). These concentrations span conditions from seawater, to exposure to deicing salts, or standing seawater that is concentrated by evaporation. When surface Cl^- concentrations rise beyond a limiting concentration, steel corrosion initiates very rapidly independent of the cover layer composition. In the 0 mass % CN CAC mortar, the corrosion delay factor diminishes to <1 at large surface Cl^- concentrations indicating performance inferior to the OPC concrete. This is due to the reduced OH^- concentration within the CAC pore solution and the high exterior Cl^- concentration overwhelming the binding capacity of the system.

Similarly, CN-dosed systems demonstrate a maximum corrosion delay factor for Cl^- concentration on the order of 0.5-to-1 mol/L, with a slight decrease as C^S_{Cl} is increased. However, even at 5 mol Cl^-/L, representative of exposure to concentrated seawater [89,90], the 30 % CN CAC layer delays corrosion by 6.7 times relative to OPC concrete. In this case, NO_3^- release due to ACE is revealed to be the critical parameter in delaying corrosion. When NO_3^- release is not considered in the 10 mass % CN CAC top-layer, the corrosion delay factor is halved, thus approaching that of the OPC concrete at high Cl^- concentrations. **This suggests that the provision of coatings capable of ACE is an efficient approach to – under suitable exposure conditions – more than double the service life of concrete infrastructure**. It should be noted, however, that the conclusions of this study are applicable to uncracked concrete, or concrete in which a surface penetrating crack does not intersect or approach the steel reinforcement. However, due to the rapid kinetics of Cl^- uptake in CAC systems [73], ACE binding is expected to exert beneficial effects even when the cover is cracked. Depending on the Cl^- exposure conditions, the ACE capacity of the CAC mortar top-layers is estimated to reach saturation within 10 years to 20 years. However, “mill-and-fill” operations could be used to periodically replace these layers, re-enhancing the ACE capacity of such top-layers. These outcomes suggest new routes to mitigate steel corrosion in concrete infrastructure.

6. Summary and conclusions

Cl^--induced corrosion of steel embedded in reinforced concrete is a major cause of premature degradation of concrete infrastructure. AFm phases present in cementitious systems are able to sequester and release anions in relation to their thermodynamic preference for interlayer site occupation [27,28]. This bestows AFm compounds with an ability for anion capture and exchange (ACE); a novel route to mitigate Cl^- penetration and resulting corrosion. Indeed, CAC formulations dosed with CN are shown to be capable of sequestering Cl^- species, while releasing corrosion inhibiting NO_3^- species [19]. Precise input data of Cl^- binding and NO_3^- exchange, and ion-diffusion rates are input into a multi-

species Nernst-Planck model to quantitatively describe the evolutions of Cl^-/OH^- and Cl^-/NO_3^- ratios in the pore solution. It is noted that across all potential combinations of diffusion coefficients, the effects of Cl^- binding and NO_3^- exchange are crucial in delaying the onset of steel corrosion – thereby enhancing service life.

As an example, in the case of seawater exposure, the provision of CAC + CN-based top-layers is estimated to increase the service life (or conversely delay the onset of steel corrosion) by a factor ranging between $5 \leq d_f \leq 10$, where d_f is the delay factor (unitless). These outcomes remain independent of the threshold values selected for corrosion risk indicators – i.e., commonly taken as $Cl^-/OH^- \geq 0.6$ and $Cl^-/NO_3^- \leq 0.25$ – as, in general, ACE is beneficial in delaying, or preventing the onset of steel reinforcement corrosion. The outcomes make a case for the use of functional ACE coatings that act as more than just a physical barrier (e.g., a sealer, or a high-performance concrete topping that only reduces ion-diffusion rates [91,92]) as an innovative means to mitigate steel corrosion related degradation of concrete infrastructure.

Acknowledgments

The authors acknowledge financial support for this research provided by: The National Science Foundation (CMMI: 1401533 and CAREER: 1235269), University of California, Los Angeles (UCLA) and Yara Industrial Nitrates. The contents of this paper reflect the views/opinions of the authors, who are responsible for the accuracy of datasets presented herein. This publication does not construe approval or disapproval by the funding agencies and does not comprise a regulation, specification, or standard. This research was carried out in the Laboratory for the Chemistry of Construction Materials (LC^2) and the core-Molecular Instrumentation Center at UCLA, and the Engineering Laboratory at the National Institute of Standards and Technology (NIST). As such, the authors acknowledge the support that has made these facilities and their operations possible. The authors thank Prof. Bruce Dunn/Jonathan Lau for access to electrochemical characterization tools. MB and GNS acknowledge Professor Fredrik P. Glasser (University of Aberdeen, Scotland) for his insights and stimulating discussions regarding ion exchange processes.

References

1. Hansson CM. The Impact of Corrosion on Society. Metall Mater Trans A. 2011; 42:2952–2962. DOI: 10.1007/s11661-011-0703-2
2. Poursaee, A. Corrosion of steel in concrete structures. 1st. Woodhead Publishing; 2016.
3. Angst U, Elsener B, Jamali A, Adey B. Concrete cover cracking owing to reinforcement corrosion–theoretical considerations and practical experience. Mater Corros. 2012; 63:1069–1077.
4. Amey SL, Johnson DA, Miltenberger MA, Farzam H. Predicting the service life of concrete marine structures: an environmental methodology. ACI Struct J. 1998; 95
5. Koch, GH., Brongers, MPH., Thompson, NG., Virmani, YP., Payer, JH. Corrosion cost and preventative strategies in the United States. NACE International; 2002.
6. Federal Highway Administration. Deficient Bridges by Highway System 2015. 2015. http://www.fhwa.dot.gov/bridge/nbi/no10/defbr15.cfm accessed July 11, 2016
7. Bertolini, L., Elsener, B., Pedeferri, P., Redaelli, E., Polder, RB. Corrosion of Steel in Concrete: Prevention, Diagnosis, Repair. John Wiley & Sons; 2013.
8. Bazant ZP. Physical model for steel corrosion in concrete sea structures—theory. J Struct Div. 1979; 105:1137–1153.
9. Broomfield, JP. Corrosion of steel in concrete: understanding, investigation, and repair. E & FN Spon; London; New York: 1997.
10. Angst U, Elsener B, Larsen CK, Vennesland Ø. Critical chloride content in reinforced concrete — A review. Cem Concr Res. 2009; 39:1122–1138. DOI: 10.1016/j.cemconres.2009.08.006
11. Hausmann DA. Steel corrosion in concrete- How does it occur? Mater Prot. 1967; 6:19–23.

12. Ann KY, Buenfeld NR. The effect of calcium nitrite on the chloride-induced corrosion of steel in concrete. Mag Concr Res. 2007; 59:689–697. DOI: 10.1680/macr.2007.59.9.689
13. Berke NS, Hicks MC. Predicting long-term durability of steel reinforced concrete with calcium nitrite corrosion inhibitor. Cem Concr Compos. 2004; 26:191–198. DOI: 10.1016/S0958-9465(03)00038-6
14. Mammoliti L, Hansson CM, Hope BB. Corrosion inhibitors in concrete Part II: Effect on chloride threshold values for corrosion of steel in synthetic pore solutions. Cem Concr Res. 1999; 29:1583–1589.
15. Ormellese M, Berra M, Bolzoni F, Pastore T. Corrosion inhibitors for chlorides induced corrosion in reinforced concrete structures. Cem Concr Res. 2006; 36:536–547. DOI: 10.1016/j.cemconres.2005.11.007
16. Reou JS, Ann KY. The electrochemical assessment of corrosion inhibition effect of calcium nitrite in blended concretes. Mater Chem Phys. 2008; 109:526–533.
17. Rosenberg, AM., Gaidis, JM., Kossivas, TG., Previte, RW. Chloride Corros Steel Concr. ASTM International; 1977. A corrosion inhibitor formulated with calcium nitrite for use in reinforced concrete. http://www.astm.org/DIGITAL_LIBRARY/STP/PAGES/STP27956S.htm accessed June 5, 2016
18. Gaidis JM. Chemistry of corrosion inhibitors. Cem Concr Compos. 2004; 26:181–189.
19. Balonis M, Glasser FP. Calcium nitrite corrosion inhibitor in portland cement: Influence of nitrite on chloride binding and mineralogy. J Am Ceram Soc. 2011; 94:2230–2241. DOI: 10.1111/j.1551-2916.2010.04362.x
20. Valcarce MB, Vázquez M. Carbon steel passivity examined in alkaline solutions: The effect of chloride and nitrite ions. Electrochimica Acta. 2008; 53:5007–5015. DOI: 10.1016/j.electacta.2008.01.091
21. Justnes H, Nygaard EC. Calcium nitrate as a multi-functional concrete admixture. Concrete. 2010; 44:34.
22. Ngala VT, Page CL, Page MM. Corrosion inhibitor systems for remedial treatment of reinforced concrete. Part 1: calcium nitrite. Corros Sci. 2002; 44:2073–2087.
23. Martıń-Pérez B, Zibara H, Hooton RD, Thomas MDA. A study of the effect of chloride binding on service life predictions. Cem Concr Res. 2000; 30:1215–1223. DOI: 10.1016/S0008-8846(00)00339-2
24. Oh BH, Jang SY. Effects of material and environmental parameters on chloride penetration profiles in concrete structures. Cem Concr Res. 2007; 37:47–53. DOI: 10.1016/j.cemconres.2006.09.005
25. Galan I, Glasser FP. Chloride in cement. Adv Cem Res. 2014; 27:63–97. DOI: 10.1680/adcr.13.00067
26. Matschei T, Lothenbach B, Glasser FP. The AFm phase in Portland cement. Cem Concr Res. 2007; 37:118–130. DOI: 10.1016/j.cemconres.2006.10.010
27. Balonis, M. Ph D Dissertation. University of Aberdeen; 2010. The influence of inorganic chemical accelerators and corrosion inhibitors on the mineralogy of hydrated portland cement systems.
28. Falzone G, Balonis M, Sant G. X-AFm stabilization as a mechanism of bypassing conversion phenomena in calcium aluminate cements. Cem Concr Res. 2015; 72:54–68. DOI: 10.1016/j.cemconres.2015.02.022
29. Birnin-Yauri UA, Glasser FP. Friedel's salt, Ca2Al(OH)6(Cl,OH)·2H2O: its solid solutions and their role in chloride binding. Cem Concr Res. 1998; 28:1713–1723. DOI: 10.1016/S0008-8846(98)00162-8
30. Hirao H, Yamada K, Takahashi H, Zibara H. Chloride Binding of Cement Estimated by Binding Isotherms of Hydrates. J Adv Concr Technol. 2005; 3:77–84. DOI: 10.3151/jact.3.77
31. Luo R, Cai Y, Wang C, Huang X. Study of chloride binding and diffusion in GGBS concrete. Cem Concr Res. 2003; 33:1–7. DOI: 10.1016/S0008-8846(02)00712-3
32. Dhir RK, El-Mohr MAK, Dyer TD. Chloride binding in GGBS concrete. Cem Concr Res. 1996; 26:1767–1773. DOI: 10.1016/S0008-8846(96)00180-9
33. Cheewaket T, Jaturapitakkul C, Chalee W. Long term performance of chloride binding capacity in fly ash concrete in a marine environment. Constr Build Mater. 2010; 24:1352–1357. DOI: 10.1016/j.conbuildmat.2009.12.039

34. Loser R, Lothenbach B, Leemann A, Tuchschmid M. Chloride resistance of concrete and its binding capacity – Comparison between experimental results and thermodynamic modeling. Cem Concr Compos. 2010; 32:34–42. DOI: 10.1016/j.cemconcomp.2009.08.001
35. Jones MR, Macphee DE, Chudek JA, Hunter G, Lannegrand R, Talero R, Scrimgeour SN. Studies using 27 Al MAS NMR of AFm and AFt phases and the formation of Friedel's salt. Cem Concr Res. 2003; 33:177–182.
36. Ampadu KO, Torii K. Chloride ingress and steel corrosion in cement mortars incorporating low-quality fly ashes. Cem Concr Res. 2002; 32:893–901. DOI: 10.1016/S0008-8846(02)00721-4
37. Bentz DP, Garboczi EJ, Lu Y, Martys N, Sakulich AR, Weiss WJ. Modeling of the influence of transverse cracking on chloride penetration into concrete. Cem Concr Compos. 2013; 38:65–74. DOI: 10.1016/j.cemconcomp.2013.03.003
38. Bentz DP, Guthrie WS, Jones SZ, Martys NS. Predicting Service Life of Steel-Reinforced Concrete Exposed to Chlorides. Concr Int. 2014; 36:55–64.
39. Jones S, Martys N, Lu Y, Bentz D. Simulation studies of methods to delay corrosion and increase service life for cracked concrete exposed to chlorides. Cem Concr Compos. 2015; 58:59–69. DOI: 10.1016/j.cemconcomp.2014.12.014
40. Jensen MM, De Weerdt K, Johannesson B, Geiker MR. Use of a multi-species reactive transport model to simulate chloride ingress in mortar exposed to NaCl solution or sea-water. Comput Mater Sci. 2015; 105:75–82. DOI: 10.1016/j.commatsci.2015.04.023
41. Samson E, Marchand J, Beaudoin JJ. Modeling the influence of chemical reactions on the mechanisms of ionic transport in porous materials: An overview. Cem Concr Res. 2000; 30:1895–1902. DOI: 10.1016/S0008-8846(00)00458-0
42. Truc O, Ollivier JP, Nilsson LO. Numerical simulation of multi-species diffusion. Mater Struct. 2000; 33:566–573. DOI: 10.1007/BF02480537
43. Samson E, Marchand J. Modeling the transport of ions in unsaturated cement-based materials. Comput Struct. 2007; 85:1740–1756. DOI: 10.1016/j.compstruc.2007.04.008
44. Sleiman H, Amiri O, Ait-Mokhtar A, Loche JM. Chloride transport through unsaturated concrete: chloride profile simulations and experimental validation. Mag Concr Res. 2012; 64:351–359. DOI: 10.1680/macr.9.00153
45. Jensen MM, Johannesson B, Geiker MR. Framework for reactive mass transport: Phase change modeling of concrete by a coupled mass transport and chemical equilibrium model. Comput Mater Sci. 2014; 92:213–223. DOI: 10.1016/j.commatsci.2014.05.021
46. Luping T, Nilsson LO. Chloride binding capacity and binding isotherms of OPC pastes and mortars. Cem Concr Res. 1993; 23:247–253.
47. Mohammed TU, Hamada H. Relationship between free chloride and total chloride contents in concrete. Cem Concr Res. 2003; 33:1487–1490. DOI: 10.1016/S0008-8846(03)00065-6
48. Balonis M, Glasser FP, Mędala M. Influence of calcium nitrate and nitrite on the constitution of AFm and AFt cement hydrates. Adv Cem Res. 2011; 23:129–143. DOI: 10.1680/adcr.10.00002
49. Le Saoût G, Kocaba V, Scrivener K. Application of the Rietveld method to the analysis of anhydrous cement. Cem Concr Res. 2011; 41:133–148. DOI: 10.1016/j.cemconres.2010.10.003
50. Guirado F, Galí S, Chinchón S. Quantitative Rietveld analysis of aluminous cement clinker phases. Cem Concr Res. 2000; 30:1023–1029. DOI: 10.1016/S0008-8846(00)00289-1
51. ASTM Standard C305-14. Standard Practice for Mechanical Mixing of Hydraulic Cement Pastes and Mortars of Plastic Consistency. ASTM International; West Conshohocken, PA: 2014.
52. ASTM Standard C778-13. Standard Specification for Standard Sand. ASTM International; West Conshohocken, PA: 2013.
53. Scrivener, KL., Capmas, A. Calcium Aluminate Cements. In: Hewlett, P., editor. Leas Chem Cem Concr. 4th. Elsevier Science & Technology Books; 2004. p. 713-782.
54. Pérez M, Vázquez T, Triviño F. Study of stabilized phases in high alumina cement mortars Part I Hydration at elevated temperatures followed by carbonation. Cem Concr Res. 1983; 13:759–770. DOI: 10.1016/0008-8846(83)90077-7
55. PSI. GEMS Selektor. 2014. http://gems.web.psi.ch

56. Kulik, D., Berner, U., Curti, E. Modelling chemical equilibrium partitioning with the GEMS-PSI code. 2004. http://www.iaea.org/inis/collection/NCLCollectionStore/_Public/36/002/36002867.pdf accessed March 1, 2015
57. Kulik DA, Wagner T, Dmytrieva SV, Kosakowski G, Hingerl FF, Chudnenko KV, Berner UR. GEM-Selektor geochemical modeling package: revised algorithm and GEMS3K numerical kernel for coupled simulation codes. Comput Geosci. 2012; 17:1–24. DOI: 10.1007/s10596-012-9310-6
58. Wagner T, Kulik DA, Hingerl FF, Dmytrieva SV. GEM-Selektor geochemical modeling package: TSolMod library and data interface for multicomponent phase models. Can Mineral. 2012; 50:1173–1195. DOI: 10.3749/canmin.50.5.1173
59. Balonis M, Glasser FP. The density of cement phases. Cem Concr Res. 2009; 39:733–739.
60. Lothenbach B, Pelletier-Chaignat L, Winnefeld F. Stability in the system CaO–Al2O3–H2O. Cem Concr Res. 2012; 42:1621–1634. DOI: 10.1016/j.cemconres.2012.09.002
61. Jappy TG, Glasser FP. Synthesis and stability of silica-substituted hydro garnet Ca 3 Al 2 Si 3-x O 12-4x (OH) 4x. Adv Cem Res. 1991; 4:1–8.
62. Dilnesa BZ, Lothenbach B, Le Saout G, Renaudin G, Mesbah A, Filinchuk Y, Wichser A, Wieland E. Iron in carbonate containing AFm phases. Cem Concr Res. 2011; 41:311–323.
63. Dilnesa BZ, Lothenbach B, Renaudin G, Wichser A, Wieland E. Stability of monosulfate in the presence of iron. J Am Ceram Soc. 2012; 95:3305–3316.
64. Filippov L, Thomas F, Filippova I, Yvon J, Morillon-Jeanmaire A. Stabilization of NaCl-containing cuttings wastes in cement concrete by in situ formed mineral phases. J Hazard Mater. 2009; 171:731–738. DOI: 10.1016/j.jhazmat.2009.06.065 [PubMed: 19631465]
65. Chu KY, Thompson AR. Densities and Refractive Indices of Alcohol-Water Solutions of n-Propyl, Isopropyl, and Methyl Alcohols. J Chem Eng Data. 1962; 7:358–360. DOI: 10.1021/je60014a011
66. Ferraris CF, Hackley VA, Avilés AI. Measurement of particle size distribution in portland cement powder: Analysis of ASTM round robin studies. Cem Concr Aggreg. 2004; 26:1–11.
67. Christensen BJ, Coverdale T, Olson RA, Ford SJ, Garboczi EJ, Jennings HM, Mason TO. Impedance Spectroscopy of Hydrating Cement-Based Materials: Measurement, Interpretation, and Application. J Am Ceram Soc. 1994; 77:2789–2804. DOI: 10.1111/j.1151-2916.1994.tb04507.x
68. Garboczi EJ, Bentz DP. Computer simulation of the diffusivity of cement-based materials. J Mater Sci. 1992; 27:2083–2092. DOI: 10.1007/BF01117921
69. Barneyback RS Jr, Diamond S. Expression and analysis of pore fluids from hardened cement pastes and mortars. Cem Concr Res. 1981; 11:279–285. DOI: 10.1016/0008-8846(81)90069-7
70. Miller, RL., Bradford, WL., Peters, NE. Specific conductance: theoretical considerations and application to analytical quality control. U.S Geological Survey; 1988. http://pubs.usgs.gov/wsp/2311/report.pdf accessed August 5, 2016
71. Adamson, AW., Gast, AP. Physical chemistry of surfaces. 5th. Wiley; 1997.
72. Sergi G, Yu SW, Page CL. Diffusion of chloride and hydroxyl ions in cementitious materials exposed to a saline environment. Mag Concr Res. 1992; 44:63–69. DOI: 10.1680/macr.1992.44.158.63
73. Puerta-Falla G, Balonis M, Falzone G, Bauchy M, Neithalath N, Sant G. Monovalent ion-exchange kinetics of hydrated calcium-alumino layered double hydroxides. J Phys Chem C Submitted. 2016
74. Caré S. Influence of aggregates on chloride diffusion coefficient into mortar. Cem Concr Res. 2003; 33:1021–1028. DOI: 10.1016/S0008-8846(03)00009-7
75. Shane JD, Mason TO, Jennings HM, Garboczi EJ, Bentz DP. Effect of the interfacial transition zone on the conductivity of portland cement mortars. J Am Ceram Soc. 2000; 83:1137–1144. DOI: 10.1111/j.1151-2916.2000.tb01344.x
76. Bentz DP, Jensen OM, Coats AM, Glasser FP. Influence of silica fume on diffusivity in cement-based materials: I. Experimental and computer modeling studies on cement pastes. Cem Concr Res. 2000; 30:953–962. DOI: 10.1016/S0008-8846(00)00264-7
77. Martys, NS. Survey of concrete transport properties and their measurement. National Institute of Standards and Technology; 1996. http://fire.nist.gov/bfrlpubs/build95/PDF/b95095.pdf accessed August 5, 2016

78. Nguyen TQ, Baroghel-Bouny V, Dangla P. Prediction of chloride ingress into saturated concrete on the basis of a multi-species model by numerical calculations. Comput Concr. 2006; 3:401u422.

79. Samson E, Marchand J. Numerical Solution of the Extended Nernst–Planck Model. J Colloid Interface Sci. 1999; 215:1–8. DOI: 10.1006/jcis.1999.6145 [PubMed: 10362465]

80. Barbarulo R, Marchand J, Snyder KA, Prené S. Dimensional analysis of ionic transport problems in hydrated cement systems: Part 1. Theoretical considerations. Cem Concr Res. 2000; 30:1955–1960. DOI: 10.1016/S0008-8846(00)00383-5

81. Friedmann H, Amiri O, Aït-Mokhtar A. Physical modeling of the electrical double layer effects on multispecies ions transport in cement-based materials. Cem Concr Res. 2008; 38:1394–1400. DOI: 10.1016/j.cemconres.2008.06.003

82. MacGillivray AD. Nernst-Planck Equations and the Electroneutrality and Donnan Equilibrium Assumptions. J Chem Phys. 1968; 48:2903–2907. DOI: 10.1063/1.1669549

83. Dickson, AG., Goyet, C. Handbook of methods for the analysis of the various parameters of the carbon dioxide system in sea water. 1994. publisher not identifiedhttp://cdiac.esd.ornl.gov/oceans/DOE_94.pdf accessed July 10, 2016

84. Taylor, HFW. Cement Chemistry. Thomas Telford; 1997.

85. Haynes, WM. CRC handbook of chemistry and physics. 96th. CRC Press; 2015.

86. Aguayo M, Yang P, Vance K, Sant G, Neithalath N. Electrically driven chloride ion transport in blended binder concretes: Insights from experiments and numerical simulations. Cem Concr Res. 2014; 66:1–10. DOI: 10.1016/j.cemconres.2014.07.022

87. Birdsall A, Guthrie W, Bentz D. Effects of initial surface treatment timing on chloride concentrations in concrete bridge decks. Transp Res Rec J Transp Res Board. 2007; 2028:103–110. DOI: 10.3141/2028-12

88. Lothenbach B, Matschei T, Möschner G, Glasser FP. Thermodynamic modelling of the effect of temperature on the hydration and porosity of Portland cement. Cem Concr Res. 2008; 38:1–18. DOI: 10.1016/j.cemconres.2007.08.017

89. Berke NS, Hicks MC. Predicting Chloride Profiles in Concrete. Corrosion. 1994; 50:234–239. DOI: 10.5006/1.3293515

90. Kassir MK, Ghosn M. Chloride-induced corrosion of reinforced concrete bridge decks. Cem Concr Res. 2002; 32:139–143. DOI: 10.1016/S0008-8846(01)00644-5

91. Żemajtis J, Weyers R. Concrete Bridge Service Life Extension Using Sealers in Chloride-Laden Environments. Transp Res Rec J Transp Res Board. 1996; 1561:1–5. DOI: 10.3141/1561-01

92. Harris D, Sarkar J, Ahlborn T. Characterization of Interface Bond of Ultra-High-Performance Concrete Bridge Deck Overlays. Transp Res Rec J Transp Res Board. 2011; 2240:40–49. DOI: 10.3141/2240-07

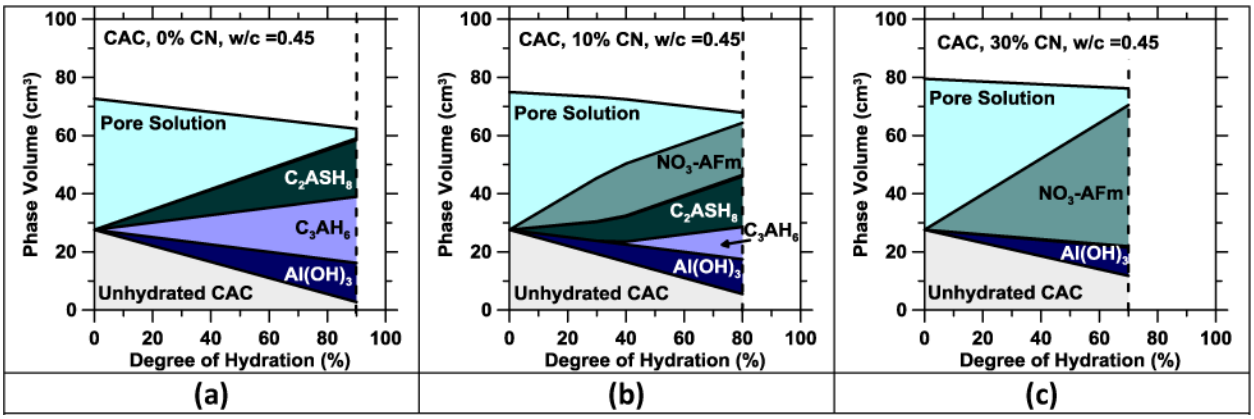

Figure 1.

The hydrated phase assemblages calculated using GEMS for CAC systems for *w/c* = 0.45 containing: **(a)** 0 mass % CN, **(b)** 10 mass % CN, and **(c)** 30 mass % CN [28]. These calculations consider 100 g of anhydrous CAC reacting with 45 g of water/CN solution. The dashed vertical line shows the maximum simulated degree of hydration for each system. At a degree of hydration greater than this value, chemical reactions will cease due to limitations on water availability.

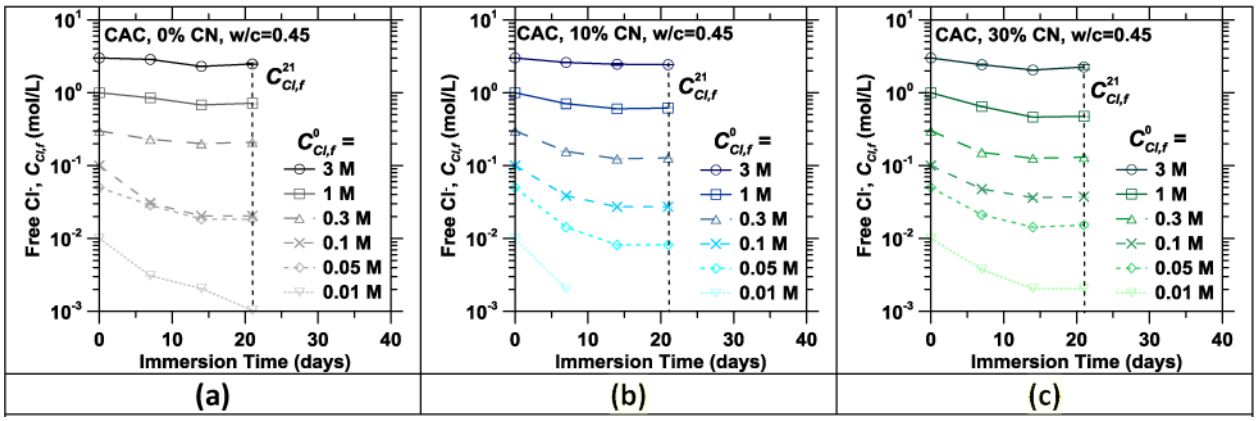

Figure 2.

The free Cl^- concentration ($C_{Cl,f}$) in solution as a function of time for $CaCl_2{\cdot}2H_2O$ solutions in contact with hydrated CAC pastes containing: **(a)** 0 mass % CN, **(b)** 10 mass % CN, and **(c)** 30 mass % CN over the concentration range: 0.01 mol/L ≤ $C^0_{Cl,f}$ ≤ 3 mol/L. The coefficient of variation of the $C_{Cl,f}$ measurements was ≈5%.

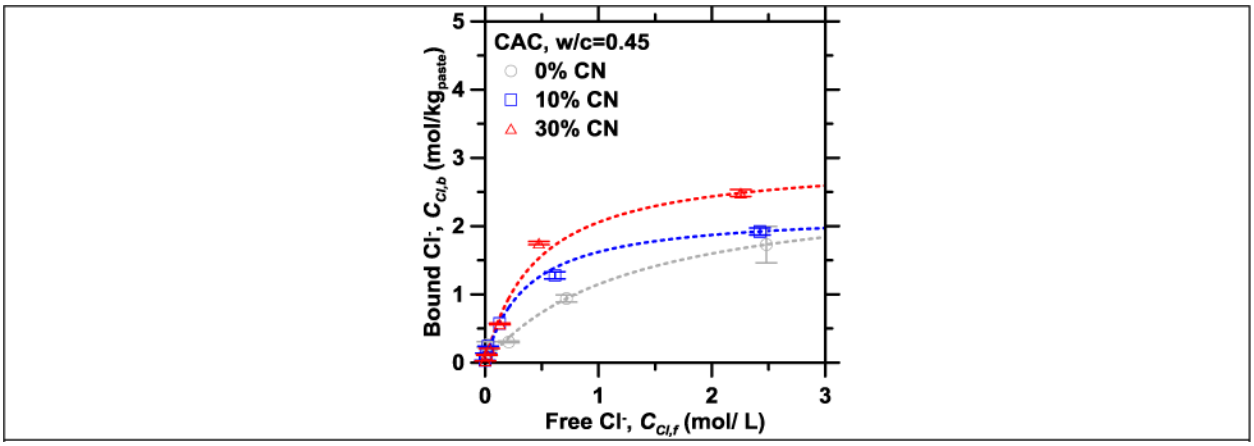

Figure 3.

The measured Cl^- binding isotherms for the hydrated CAC pastes following 21 d of immersion in $CaCl_2 \cdot 2H_2O$ solutions. The error bars indicate ± one standard deviation in the experimental measurements, which were performed in triplicate.

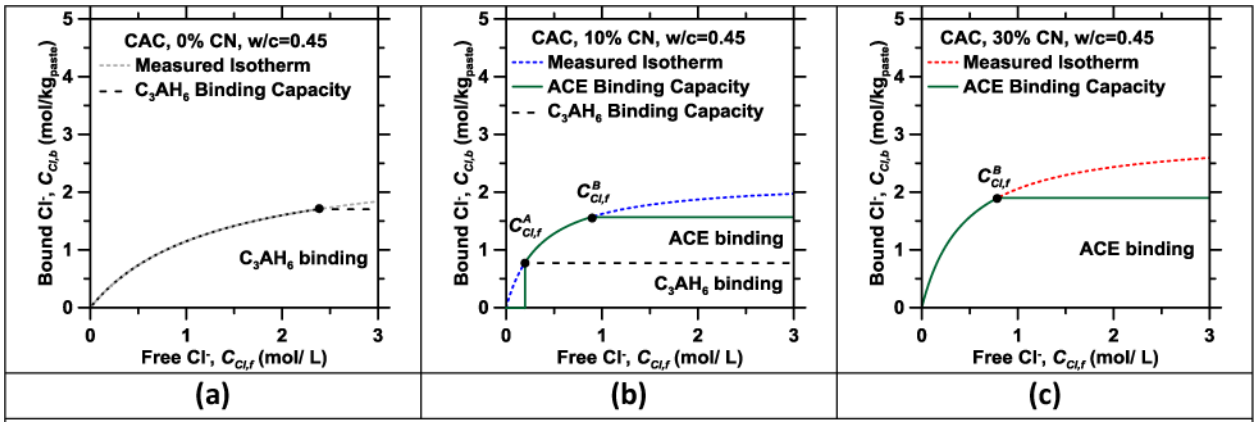

Figure 4.

A representation of the different contributions to Cl^- binding which describe the uptake capacity of hydrated CAC pastes containing: **(a)** 0 mass % CN, **(b)** 10 mass % CN, and **(c)** 30 mass % CN.

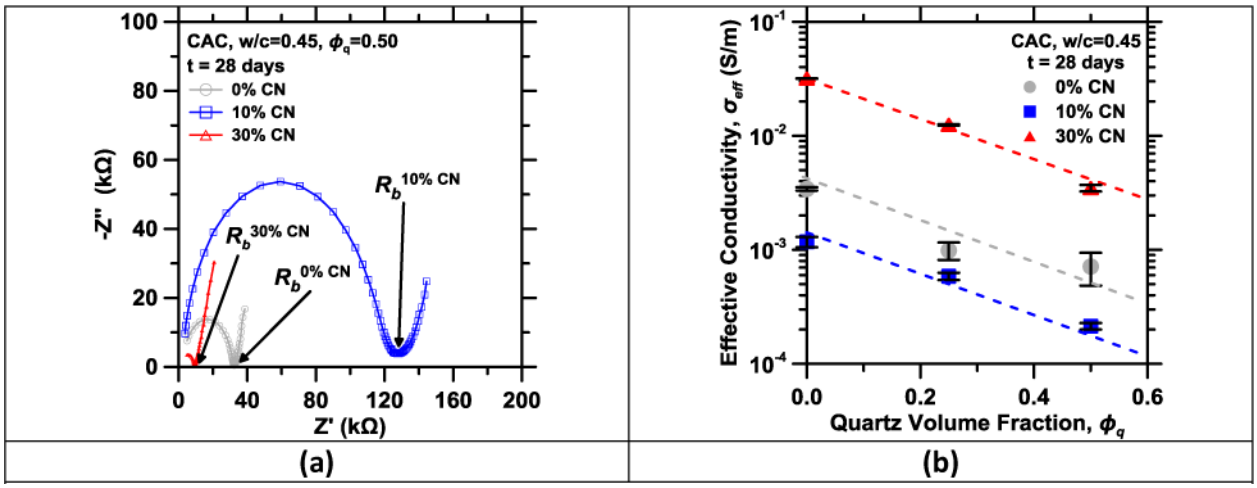

Figure 5.

(a) A Nyquist plot obtained from EIS measurements depicting the bulk resistance (R_b, kΩ) of the hydrated CAC + CN mixtures (ϕ_q =0.50). **(b)** The effective conductivity of hydrated CAC + CN mixtures as a function of the quartz dosage. The data points represent the average of two replicates, with error bars indicating the upper and lower values.

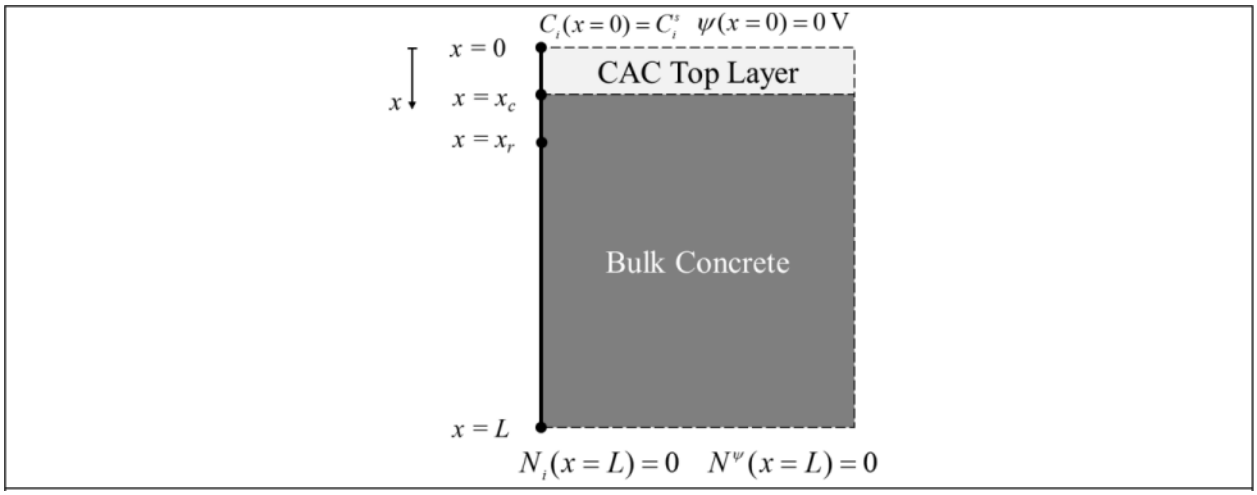

Figure 6.

A schematic of the simulated concrete bridge-deck section subject to Cl^- ingress at ($x = 0$) that features a CAC-based top-layer of thickness x_c.

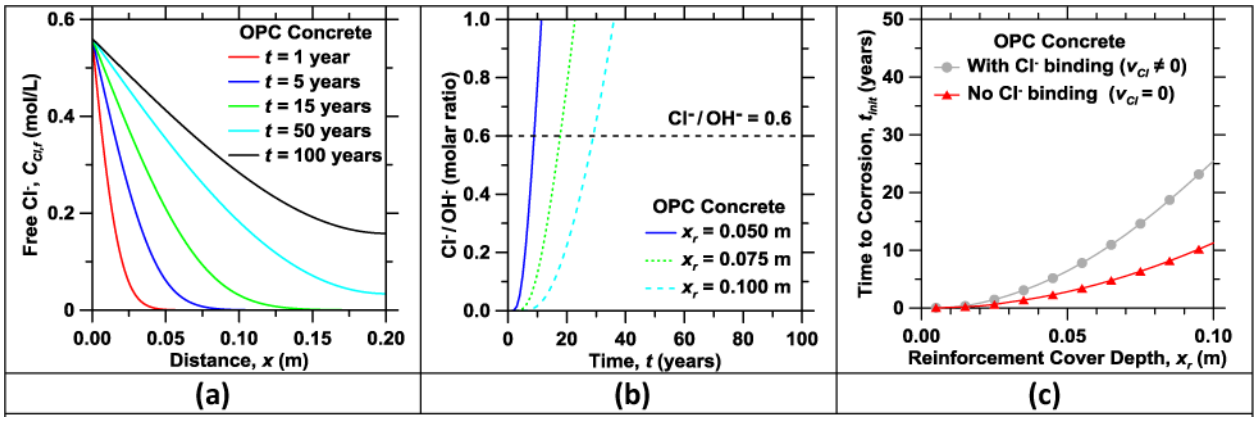

Figure 7.

(a) The simulated Cl^- concentration profiles within the OPC concrete, and, **(b)** The Cl^-/OH^- ratio within an OPC concrete as a function of time for different cover depths. The dashed line indicates the critical Cl^-/OH^- ratio at which steel corrosion initiates. **(c)** The calculated time to corrosion initiation (t_{init}) as a function of the reinforcement cover depth x_r.

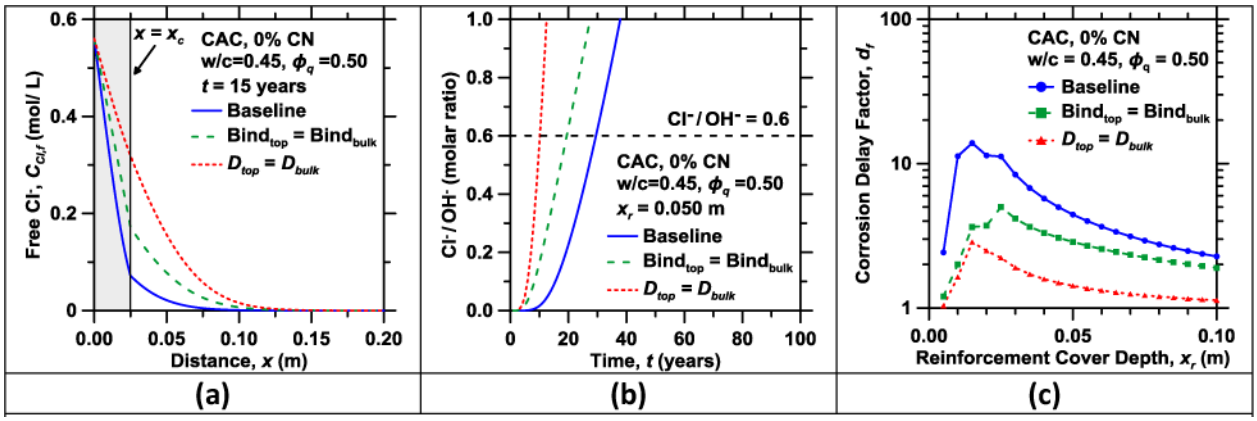

Figure 8.

(a) The simulated Cl^- concentration profiles within an OPC concrete topped with a 0 mass % CN CAC top-layer (ϕ_q = 0.50, x_c=0.025 m) after 15 years of exposure to seawater. The dashed lines show scenarios wherein a Cl^- binding isotherm equal to that of the OPC paste was assumed in the CAC top-layer ($Bind_{top} = Bind_{bulk}$), or, wherein the CAC top-layer and the OPC concrete are assumed to have similar ionic diffusivities ($D_{top} = D_{bulk}$). **(b)** The Cl^-/OH^- ratio as a function of time at a cover depth x_r = 0.050 m. The horizontal dashed line in **(b)** indicates the critical Cl^-/OH^- ratio when steel corrosion initiates. **(c)** The corrosion delay factor (d_f) produced by replacement of the OPC concrete with a 0 mass % CN CAC top-layer, as a function of reinforcement cover depth x_r.

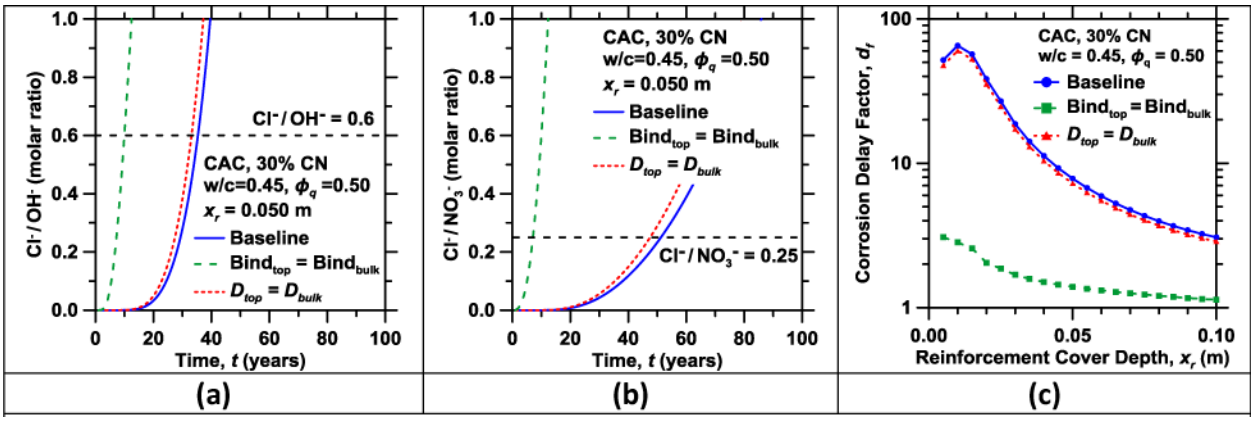

Figure 9.

(a) The Cl^-/OH^- ratio, and, **(b)** The Cl^-/NO_3^- ratio within OPC concrete topped with a 30 mass % CN CAC top-layer (ϕ_q = 0.50, x_c=0.025 m) as a function of time for a cover depth x_r = 0.050 m. The horizontal dashed lines in **(a)** and **(b)** indicate the critical Cl^-/OH^- and Cl^-/NO_3^- ratios for the initiation of steel corrosion or inability for the re-passivation of steel by NO_3^-. **(c)** The corrosion delay factor (d_f) produced by replacing OPC concrete with a 30 mass % CN CAC top-layer, as a function of reinforcement cover depth x_r.

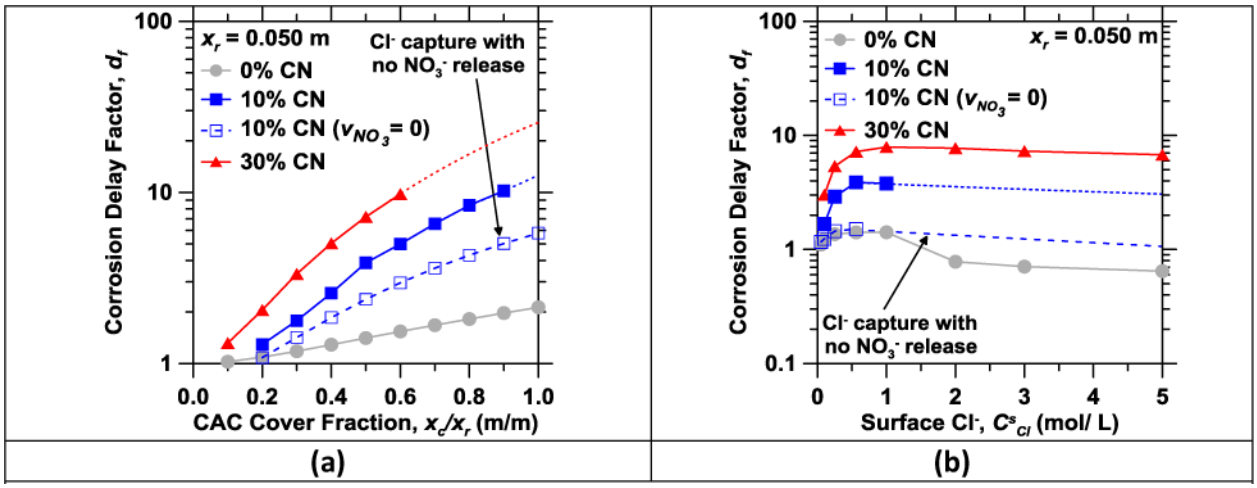

Figure 10.

The corrosion delay factor relative to OPC concrete as a function of: **(a)** The fractional thickness of the CAC top-layer (x_C/x_I), and **(b)** The surface Cl^- concentration (C^S_{Cl}), for a reinforcement cover depth x_r = 0.050 m.

Table 1

The ion-dependent diffusion coefficients at infinite dilution (D_i^{inf}) at T = 25 °C [85], the boundary conditions (i.e., concentrations of each ionic species at the exposed surface; x = 0 m, with C_i^s corresponding to seawater [83]), and the initial conditions of the simulations (i.e., the concentrations of ions within the pore solution of each cementitious matrix).

Ionic Species	D_i^{inf} (10^{-9} m^2/s)	C_i^s (mmol/L)	$C_i^{0\%CN}$ (mmol/L)	$C_i^{10\%CN}$ (mmol/L)	$C_i^{30\%CN}$ (mmol/L)	C_i^{OPC}* (mmol/L)
Na^+	1.33	480	0	0	0	140
K^+	1.96	10	0	0	0	210
Ca^{2+}	0.793	10	23.1	23.2	57.1	0
Mg^{2+}	0.705	53	0	0	0	0
$Al(OH)_4^-$	1.04	0	20.0	20.0	20.0	0
OH^-	5.27	0.0013	26.1	24.5	7.8	330
Cl^-	2.03	560	0	0	0	0
NO_3^-	1.90	0	0	1.9	86.3	0
SO_4^{2-}	1.07	29	0	0	0	10

*Aguayo et al. [86]

Table 2

The material-specific input parameters representing: Cl^- binding, formation factor (i.e., which dictates ion diffusion rates within a constrained microstructure), and the mixture compositions (i.e., the porosity and paste content of the CAC mortars and OPC concrete).

Material	α (L/kgpaste)	β (L/mol Cl^-)	Binding rate constant, k_{Cl} (s^{-1})	σ_{eff}/σ_0	Porosity (ϕ_p)	Paste content (kg/m^3 concrete)
CAC + 0% CN	0.00204	0.00077	1×10^{-7}	1.14×10^{-3}	0.14	870
CAC + 10% CN	0.00608	0.00275	1×10^{-7}	3.50×10^{-4}	0.09	970
CAC + 30% CN	0.00661	0.00222	1×10^{-7}	3.68×10^{-3}	0.06	1020
OPC Concrete	0.00352 *	0.00416 *	1×10^{-7}	4.0×10^{-3} †	0.11 ‡	920

*Dhir et al. [32],

†Bentz et al. [76],

‡Birdsall et al. [87].